RSC Advances

PAPER

View Article Online
View Journal | View Issue

Cite this: *RSC Adv.*, 2026, **16**, 1382

Fabrication, structural analysis, and bioactivity assessment of a novel reduced graphene oxide reinforced ternary metal oxide (rGO-ZnO-SnO_2-Fe_2O_3) nanocomposite

Sirajul Haq, *[ab] Misbah Ashravi,[c] Abdurahman Hajinur Hirad,[d] Jamoliddin Razzokov,[aef] Maria Rashid,[c] Shafia Shujaat,[c] Ifza Ahmad[c] and Abdus Samad[g]

The goal of the current research was to prepare an effective hybrid material, which was expected to counter antibiotic-resistant bacterial strains and stabilize generated free radicals. For this purpose, ZnO-SnO_2-Fe_2O_3 (ZSF) and rGO-ZnO-SnO_2-Fe_2O_3 (rGO-ZSF) nanocomposites were synthesized and were calcined at 450 °C. Initially, GO was synthesized *via* a modified Hummers' method from commercially available graphite flakes and a chemical precipitation method was used to synthesize ZSF and rGO-ZSF nanocomposites. Fourier-transform infrared spectroscopy was conducted to analyze the chemical compositions of all synthesized samples. Morphological examinations were made *via* scanning electron microscopy, where the metal oxide was seen to implant in the GO sheets, and the average particle size for ZSF is 16.02 nm and for rGO-ZSF is 22.5 nm. Crystallographic properties, *i.e.* crystallite sizes, lattice strain, dislocation density (ρ) and microstrain (ε), were extracted using an X-ray diffractometer, showing a clear variation in the crystallite sizes and microstrain. The antibacterial activities of the synthesized samples were assessed against Gram-positive (G +ve) and Gram-negative (G −ve) microorganisms using the agar well diffusion technique. rGO-ZSF has significantly higher antibacterial activity than pure GO and the ZSF nanocomposite. When compared to G −ve bacteria, G +ve bacteria showed more resistance to the samples; this might be due to differences in the cell wall composition. Upon increasing the sample dose in the system, activity was observed to rise. Likewise, these samples were also employed as stabilizing agents against ABTS and DPPH free radicals, and the highest activity was achieved at higher concentrations. The IC_{50} values show that the synthesized samples showed more activity against DPPH as compared to ABTS free radicals.

Received 2nd September 2025
Accepted 3rd December 2025

DOI: 10.1039/d5ra06581j

rsc.li/rsc-advances

1 Introduction

Drug-resistant microbial species cause infectious diseases, increase the rate of mortality and morbidity, and are hazards all over the world. To minimize the death rate of people, infection-control initiatives and anticipatory operations against multidrug-resistant bacteria must be introduced.[1] Because of the overuse and exploitation of a wide range of antibiotics, disease-causing bacteria have produced drug-resistant strains that defy scientific therapy. Antimicrobial resistance in microorganisms has been labelled a global risk to human health. Consequently, the advancement of nanotechnology and the manufacturing of nanoparticles as efficient methods for treating infectious illnesses and combating antibiotic-resistant bacteria have been a focus.[2] Reactive oxygen species (free radical)-mediated damage to biological macromolecules has been related to a number of disorders, including cancer, inflammation, and neurological disease.[3] In order to attain equilibrium, free radicals from various chemical sources must steal electrons from other molecules, which degrades substrates. They develop inside organisms, are incredibly reactive, and have the power to obliterate compounds with a short lifespan.[4]

[a]*Institute of Fundamental and Applied Research, National Research University TIIAME, Kori Niyoziy 39, 100000 Tashkent, Uzbekistan. E-mail: cii_raj@yahoo.com*
[b]*Department of Information Technologies, Tashkent International University of Education, Imom Bukhoriy 6, 100207 Tashkent, Uzbekistan*
[c]*Department of Chemistry, University of Azad Jammu and Kashmir, 13100 Muzaffarabad, Pakistan*
[d]*Department of Botany and Microbiology, College of Science, King Saud University, P. O. Box.2455, Riyadh, 11451, Saudi Arabia*
[e]*Department of Biotechnology, Tashkent State Technical University, Universitet 2, Tashkent 100095, Uzbekistan*
[f]*Department of Natural Sciences, Karshi State Technical University, Mustaqillik Avenue Street 225, Kashkadarya 180100, Uzbekistan*
[g]*School of Material Science and Engineering, Nanjing Tech University, P.R China*

Researchers are looking for novel antibacterial medications to prevent the spread of infectious illness brought on by numerous dangerous bacteria and improved antibiotic resistance. Recently, nanoscale materials have emerged as innovative antibacterial agents in the current context because of their distinctive features. Various metal oxide nanoparticles (MO NPs) and graphene-based nanocomposites are utilized for combating bacterial infections.[5] Inorganic materials have appealed to researchers in the last decade since they have been shown to be safe for humans. Recently, a wide variety of MO NPs has been discovered to exhibit significant antioxidant, anti-inflammatory, and antimicrobial action. Integrating graphene nanosheets with other inorganic materials to make hybrid nanocomposites is of great interest in different fields. These graphene-based M/MO NCs are useful for medication delivery, hazardous metal ion elimination, and other applications.[6]

M/MO NPs possess unique properties due to their small sizes and high surface-to-volume ratios, enabling frequent interactions with microbes and enhancing their antibacterial effectiveness.[7] Because of certain properties, such as crystallinity, size, composition and shape, MO NPs are in increasing demand for use in modern technology and medicine throughout the world.[8,9] In recent years, the antibacterial and antioxidant properties of MO NPs have been investigated.[10] In recent decades, mono-, bi-, and tri-metallic nanoparticles have gained significant attention due to their diverse applications. Compared to mono- and bimetallic nanoparticles, tri-metallic NPs exhibit adjustable and enhanced properties due to the incorporation of a second and third metal into the nanoparticle system.[11] Trimetallic nanoparticles have a highly active surface because of rapid electron transport and crystal flaws, which makes important applications possible.[12]

GO is an intriguing substrate for attaching M/MO NPs because of its unique properties and lack of toxicity to human cells. Graphene, with a thick honeycomb crystal structure made up of a monolayer of carbon atoms, has gotten a lot of attention.[5] Graphene and its derivatives have a huge specific surface area, and great thermal, mechanical and electrical properties. The –OH, epoxy, and –COOH functional groups found in graphene oxide are useful in the fields of bacterial toxicity and medicine. Active sites for electrostatic functionalization with metals and metal oxides are produced by adding more oxygen-containing functional groups to GO. The antibacterial activity of MO NPs dispersed on GO sheets against microbes was extensive, and this also has the potential to show both catalytic and antioxidant activity. GO is a great starting point for a range of metal composites used in catalytic and biological applications.[13]

GO may be made by intercalating and oxidizing graphite powder. GO is synthesized by the oxidation of graphite using various methods, including Brodie, Staudenmaier, Hoffmann and Hummers' methods. The improvements made by Hummers to make the procedure safer include using $KMnO_4$ as an oxidant rather than $KClO_3$ which produces toxic ClO_2 gas. The Hummers approach is the one that is commonly utilized to manufacture GO since it is safer and more scalable.[14] For the synthesis of GO–MO NCs, *ex situ* hybridization and *in situ* crystallization are the two most-used manufacturing procedures. The *ex situ* method combines produced nanoparticles in a solution with graphene-based nanosheets. Graphene slips and the apparent alteration of nanocrystals frequently occur prior to mixing in order to help the components engage *via* non-covalent interactions or chemical binding. By using functionalization to regulate nucleation sites on GO, *in situ* crystallization may produce consistent nanocrystal coverage.[15]

This study aimed to synthesize biologically potent novel compounds and assess their potential for various biological applications. The selection of components for the GO-trimetallic nanocomposite was made after a literature survey and, to the best of our knowledge, this combination of metal oxides with GO is yet to be reported. The GO was prepared by a revised Hummers' method and chemical approach, *i.e.* an *ex situ* hybridization technique was utilized for the GO-ZSF and ZSF NCs. These synthesized nanocomposites were calcined at 450 °C and characterized by FTIR, SEM and XRD. The antibacterial potential of the nanocomposites was studied using *Escherichia coli* (*E. coli*) and *Staphylococcus aureus* (*S. aureus*) bacteria. This dual-strain approach was strategically chosen to assess the broad-spectrum potential of the nanoparticles, as Gram-positive and Gram-negative bacteria possess fundamentally different cell wall structures.[16] Similarly, the antioxidant activity was also assessed using ABTS and DPPH radical scavenging assays. According to the findings, the manufactured nanocomposites have a high effectiveness in killing microorganisms and scavenging free radicals. A comparison was made between the physicochemical and biological properties of uncalcined and calcined samples.

2 Materials and methods

2.1 Materials

Graphite flakes (≥99%), concentrated sulphuric acid (H_2SO_4; 98%), hydrogen peroxide (H_2O_2; 30%), potassium permanganate ($KMnO_4$; ≥99%), methanol (≥99.9%), tin chloride 2-hydrate ($SnCl_2 \cdot 2H_2O$; 98%), zinc sulphate heptahydrate ($ZnSO_4 \cdot 7H_2O$; 99%), ferric sulphate heptahydrate ($FeSO_4 \cdot 7H_2O$; ≥99%), and deionized water were among the reagents used in the study. All the used reagents and solvents were purchased from Sigma-Aldrich and used without further purification.

2.2 Methods

2.2.1 Preparation of GO. The GO was made by modifying Hummers' method, where 99 mL of H_2SO_4 was blended with 11 mL of H_3PO_4 in a 9 : 1 volume ratio. The mixture was stirred in an ice bath to maintain the temperature at 10 °C for 10 min. Then, 2 g of graphite and 8 g of $KMnO_4$ were added to the mixture and it was continuously stirred for 6 h. After the appearance of a dark green color, 6 mL of H_2O_2 was added to the reaction mixture to remove excess $KMnO_4$, and agitation was continued for 10 min. This step needs intense care as this is an exothermic process where a lot of energy is generated. After cooling to room temperature, 13 mL of HCl and 39 mL of deionized water at a volume ratio of 1 : 3 were added to the

reaction mixture, which was then centrifuged at 4000 rpm. To get to pH 7, the residue was rinsed three times using deionized water. After filtration, the suspension was dried for 24 h at 90 °C in an electric oven. The dried black GO powder was stored in an airtight polyethylene bottle.

2.2.2 Synthesis of ZSF NC. For the preparation of ZSF, 3.78 g of $SnCl_2 \cdot 2H_2O$, 4.97 g of $FeSO_4 \cdot 7H_2O$, and 4.37 g of $ZnSO_4 \cdot 7H_2O$ were added into separate beakers containing a mixture of DIW (50 mL) and methanol (10 mL). Then, 2 M NaOH solution was added to the reaction mixture to bring the pH down to 10 and the mixtures were then agitated for 30 min at 50 °C, leading to the formation of stable suspensions. To prepare ZSF, all three suspensions were mixed in a beaker and stirred (300 rpm) for 4 hours at 50 °C. The mixture was then filtered after being rinsed three times with DIW. The final product was dried in an electric oven at 100 °C and subsequently calcined at 450 °C for 2 h in a muffle furnace.

2.2.3 Synthesis of rGO-ZSF NC. For the fabrication of rGO-ZSF, 3.78 g of $SnCl_2 \cdot 2H_2O$, 4.97 g of $FeSO_4 \cdot 7H_2O$ and 4.37 g of $ZnSO_4 \cdot 7H_2O$ were added into individual beakers containing 50 mL of DIW and 10 mL of methanol. To keep the pH at 10, 2 M NaOH was introduced into these solutions and the mixtures were then agitated for 30 min at 50 °C to obtain stable suspensions. Then, 1 g of GO was ultrasonically dispersed in 100 mL of DIW and stirred for 2 h to obtain rGO. The already prepared suspensions were then slowly added to the GO suspension, which was vigorously stirred for 6 h. The mixture was then seasoned for 24 h, followed by filtration after being rinsed with DIW thrice. After drying the residue at 100 °C in an electric oven, half of the final product was subjected to calcination at 450 °C for 2 h in a muffle furnace.

2.2.4 Physicochemical characterization. To determine the functional groups on the sample surface, an FTIR spectrometer (model: Nicolet 6700 (USA)) was employed, covering a spectral range of 4000 to 400 cm^{-1}. Using a Cu source and Panalytical X-Pert Pro apparatus, XRD patterns in the 20–70° range were recorded for ZSF and rGO-ZSF. The crystallographic parameters, *i.e.* crystallite size, microstrain and dislocation density, were calculated through the W–H method (S1, S2 and S3). The sample was wrapped in adhesive carbon tape before being subjected to morphological investigation using a SEM (model: 5910 (Japan)). The microstructure and surface characteristics were examined using a JEOL JSM-5600LV scanning electron microscope (SEM) manufactured in Tokyo, Japan.

2.2.5 Antibacterial assays. The agar well diffusion assay was used to investigate the antibacterial potential of calcined and uncalcined ZSF and rGO-ZSF nanocomposite samples. *E. coli* and *S. aureus* were used. The microorganisms were obtained from Department of Biotechnology, UAJ&K, Muzaffarabad. To avoid contamination, *E. coli* and *S. aureus* were uniformly distributed over freshly prepared agar medium in sanitized culture dishes and coagulated under continuous flow at room temperature. Six wells per Petri dish were created using a sterile tip (5 mm), and the agar plug was removed with a sterilized needle. Various concentrations (10, 20, 30, 40, 50 and 60 mg in 3 mL of DIW) of each stock suspension of calcined and uncalcined ZSF and rGO-ZSF nanocomposite were poured into the wells and cultivated at 37 °C for 16 h. The antibacterial potential was assessed by determining the inhibitory zone in millimeters. Similarly, the antibacterial effects of rGO, graphite, and calcined samples of ZSF and rGO-ZSF nanocomposites were compared by pouring 30 μl from suspensions containing 60 mg^{-1} 3 mL^{-1} into four wells, while an antibiotic and water were utilized as the standard and blank, respectively. The same procedure was repeated to compare the antibacterial activities of rGO, graphite, and uncalcined ZSF and rGO-ZSF nanocomposites. All Petri plates were placed in an incubator for 24 h. The activity of each nanocomposite was assessed after 24 h by measuring the inhibitory zone in mm.

2.2.6 Antioxidant assay. The antioxidant activities of calcined and uncalcined ZSF and rGO-ZSF nanocomposites were evaluated by performing ABTS and DPPH radical scavenging assays. Various concentrations (1, 2, 3, 4, 5 and 6 mg in 5 mL of DIW) of calcined and uncalcined samples were ultrasonicated for 30 min to create uniform dispersions. ABTS free radicals were generated by agitating 5 mM potassium persulphate with 14 mM ABTS and allowing the reaction to proceed in darkness for 16 h. In order to create DPPH stock solution, 4 mg of DPPH was dissolved in 50 mL of methanol and left to stand for half an hour. The absorbance was measured at 517 nm and 734 nm using the same amount of ascorbic acid as a reference.

2.2.6.1 DPPH free radical scavenging. For a typical experiment, 50 μl of either an uncalcined or calcined sample of ZSF or rGO-ZSF was used. Each test tube included 1 mL of DDPH solution mixed with nanocomposite, which was then left to incubate for 30 minutes at room temperature. Using a UV-visible spectrophotometer, the reaction mixture's optical absorption at 517 nm was calculated, while deionized water was kept in the reference cell.

2.2.6.2 ABTS free radical scavenging. To check the radical scavenging activity against ABTS, 50 μl of either uncalcined or calcined ZSF or rGO-ZSF nanocomposite was mixed with 1 mL of $ABTS^{\bullet+}$ solution in separate experimental vessels, which were then retained at room temperature for 30 minutes. The absorbance of the sample was then observed at 734 nm using a UV-visible spectrophotometer, and methanol was placed in the reference cell.

2.2.6.3 Percentage radical scavenging activity. The percentage scavenging activities of uncalcined and calcined ZSF and rGO-ZSF nanocomposites at different concentrations were calculated as follows (A_0 = absorbance of control; A_i = absorbance of test material):

$$\%\ \text{scavenging potential} = \frac{A_0 - A_i}{A_0} \times 100 \quad (1)$$

3 Results and discussion

3.1 XRD study

3.1.1 XRD analysis of rGO. The crystalline structures and chemical compositions of synthesized GO, the tri-metallic nanocomposite and the GO-based tri-metallic composite were examined using XRD techniques. The XRD spectrum presented in Fig. 1 displays a diffraction peak at 11.01°, corresponding to an interlayer *d*-spacing of 8.18 Å, which is closely aligned with

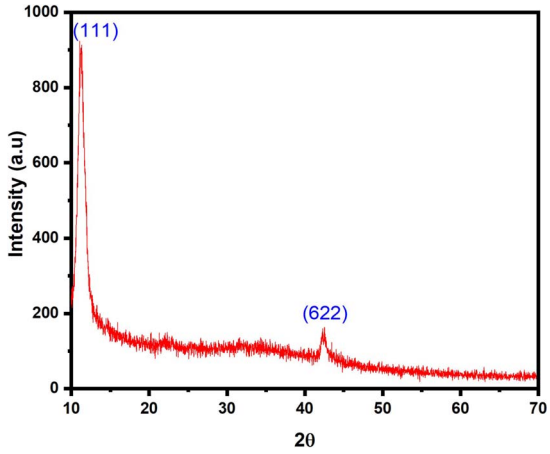

Fig. 1 The XRD pattern of reduced graphene oxide (rGO).

previously reported values. This diffraction peak is associated with the (111) plane, as indicated in reference card number 01-082-2261. The calculated density was 2.12 g cm^{-3}, while the cell volume was measured as 2834.35 × 10^6 pm^3. Besides this, another peak present at 42.43° due to the (622) plane is due to graphite, with an interatomic distance of 2.14 Å. The presence of this peak suggests that a lesser amount of graphite is still present in the sample.

3.1.2 XRD analysis of uncalcined and calcined ZSF NCs. The crystalline structure of the tri-metallic oxide nanocomposite comprising Fe_3O_4, SnO_2 and ZnO was studied through XRD analysis, and the diffractograms of both uncalcined and calcined tri-metallic oxide nanocomposites are depicted in Fig. 2. The reflection peaks at 35.06, 37.09 and 42.57° arise due to the (311), (222) and (400) diffraction planes, respectively, corresponding to the reference card 01-079-1849. The data reveals that magnetite (Fe_3O_4) forms in cubic form with the space group of Fd_3M. The size of the Fe_3O_4 crystallites is found to be 57.93 nm with 0.419% lattice strain. The ε and ρ values were found to be 2.2 × 10^{-3} and 2.98 × 10^{-4} nm^{-2}, respectively. The diffraction bands with *hkl* values of 18.40(001), 29.92(101) and 61.99(202)°, matching with the reference card 01-072-1012, are due to SnO_2 with square-based geometry with the space group of *P*4/*nmm*.[17] The SnO_2 crystal size is determined to be 35.33 nm with 0.256% imperfection. The determined ε and ρ values are 6.6 × 10^{-3} and 8.02 × 10^{-4} nm^{-2}, respectively. The diffraction bands at 2-theta positions of 31.96(101), 36.38(101) and 56.40(110)°, matching with the reference card 01-079-0205, suggest the formation of hexagonal-shaped ZnO crystallites with the space group of $P6_3mc$. The calculated crystallite size, lattice strain, ε and ρ values are 29.56 nm, 0.419%, 4.9 × 10^{-3} and 1.1458.02 × 10^{-3} nm^{-2}, respectively.

3.1.3 XRD analysis of uncalcined and calcined rGO-ZSF NCs. The crystalline structure of prepared rGO-ZSF was studied *via* XRD, and the obtained XRD patterns are shown in Fig. 3. The peaks at 32.67 and 58.18° with Miller indices of (101) and (200), respectively, are compared with information from the reference card (01-076-2378) and attributed to hexagonal-shaped carbon oxide. The size of GO was found to be 24.10 nm with a dislocation density of 1.722 × 10^{-3} nm^{-2} and ε value of 6.11 × 10^{-3}. These peaks confirm the presence of carbon-based material (GO) in the sample. The Bragg's reflections with peaks at 29.50(220), 42.66(400), and 53.70(422)° match with the JCPDS card 01-079-1849, and are assigned to magnetite (Fe_3O_4) with cubic geometrical shape with the space group of Fd_3M. 21.15 nm, 7.35 × 10^{-3}, and 2.237 × 10^{-4} nm^{-2} are the crystallite size, ε and ρ values of Fe_3O_4, respectively. The bands at 34.91, 36.46, 46.83, and 56.25° arise due to (002), (101), (102) and (110) planes, confirming the formation of six-sided ZnO crystallites with the symmetry group of $P6_3mc$. All this complements the reference card 01-079-0205.[18] The values of other parameters, *i.e.* crystallite size, ε and ρ, are found to be 17.31 nm, 7 × 10^{-3} and 3.341 × 10^{-3} nm^{-2}, respectively. The bands at 52.75 and 61.48° for the (101) and (222) planes suggest the formation of SnO_2 with orthorhombic geometrical shape, as per JCPDS card 00-029-1484.[17] The crystallite size is 15.25 nm, ε is 35.42 and ρ is 4.303 × 10^{-3} nm^{-2}. The presence of all these peaks in the XRD pattern suggest the successful formation of a tri-metallic oxide-rGO composite comprising GO sheets, ZnO, SnO_2 and Fe_3O_4.

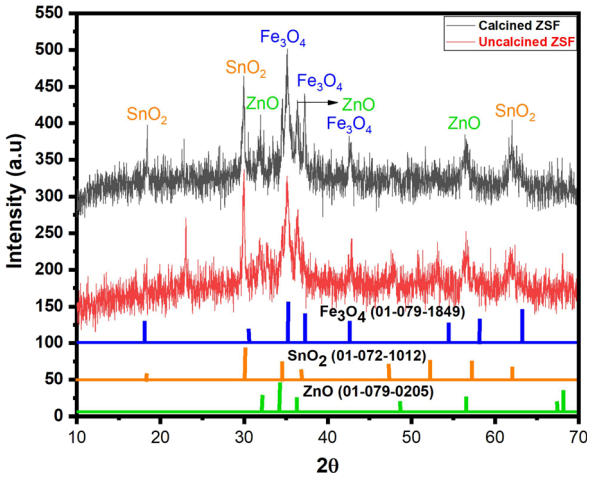

Fig. 2 The XRD patterns of uncalcined and calcined ZSF NCs.

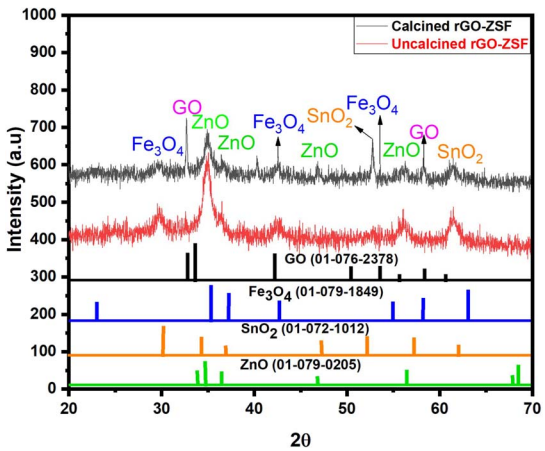

Fig. 3 XRD patterns of uncalcined and calcined rGO-ZSF NCs.

3.2 Compositional analysis

To study the bond structure and chemical composition of rGO, and ZSF and rGO-ZSF nanocomposites, FTIR analysis was carried out using KBr pellets, and spectra were acquired in transmission mode in the range of 4000 to 400 cm^{-1}.

3.2.1 FTIR analysis of rGO. In the FTIR spectra of rGO (Fig. 4), bands at 2918.19 cm^{-1} and 2873.80 cm^{-1} demonstrated, respectively, even and uneven elongation of C–H bonds.[19] The C=C bonds of aromatic groups were confirmed by the presence of a peak at 1587 cm^{-1}.[20] The C–O group was represented by a peak at 1043.22 cm^{-1}.[21] Stretching vibrations of C–O and O–H bending vibrations from carboxylic acid are represented by the peaks at 946.92 cm^{-1} and 1402.36 cm^{-1}.[22]

3.2.2 FTIR analysis of uncalcined and calcined ZSF NCs. The FTIR spectrum of uncalcined ZSF (Fig. 5) possesses a broad band centered at 3383.94 cm^{-1} reflecting the stretching vibration of a hydroxyl group connected to a metal center, along with a peak at 1631.49 cm^{-1} indicating the bending vibration of a hydroxyl group.[23] The out-of-plane O–H vibrations are evident from the band appearing at 1366.96 cm^{-1}, and the terminal OH group is represented by the band at 1115.69 cm^{-1}.[24] Metal–oxygen bridging is represented by the peaks at 1069.08 cm^{-1} and 974.97 cm^{-1}, whereas the bands at 740.22 cm^{-1} and 706.73 cm^{-1} are ascribed to O–M–O and M–O–M, respectively.[8] The Zn–O vibration was represented by the peak observed at 685.24 cm^{-1} [25] whereas the band at 621.52 cm^{-1} is attributed to the Fe–O vibration.[26] A band at 557.05 cm^{-1} represents the Sn–O vibration.[27] In comparison to uncalcined ZSF, the intensity of the bands representing the water/hydroxyl vibrations diminishes, implying that water molecules are removed from the sample and hydroxides are converted into oxides.[28]

3.2.3 FTIR analysis of uncalcined and calcined rGO-ZSF NCs. The FTIR spectrum of calcined rGO-ZSF (Fig. 6) exhibits a small band at 3555.45 cm^{-1} and a wide band in the range of 3491–3195 cm^{-1}, ascribed to non-bonding water molecules and the stretching of the hydroxyl group, along with a peak at 1643.11 cm^{-1} from the deflection vibration of the O–H moiety.[2] The band at 1478.1 cm^{-1} related to the deformation of incorporated surfactant CH_2 and CH_3.[29] The peak at 1367.4 cm^{-1} indicates aromatic ring stretching.[30,31] The bending vibration and the overlapping of carbonyl groups were represented by absorption peaks at 1080.94 cm^{-1}.[21] The band at 724.58 cm^{-1} corresponds to M–O–M vibration. The bands at 660.47 cm^{-1}, 589.40 cm^{-1} and 562.05 cm^{-1} are attributed to Zn–O, Fe–O and Sn–O vibrations, respectively.[32,33] The decrease in the hydroxyl group vibration peak after calcination implies the evaporation of water molecules from the sample. The change in particle size as a function of the calcination temperature might explain the shifting of peaks after calcination. Upon raising the calcination temperature, the nanocomposite peaks became smoother, indicating an increase in crystallinity.[34]

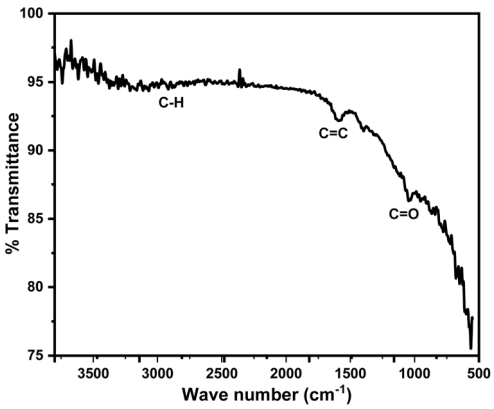

Fig. 4 The FTIR spectrum of rGO.

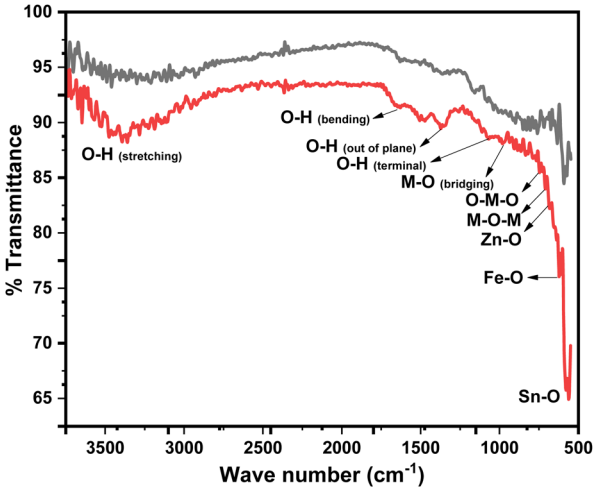

Fig. 5 FTIR spectra of uncalcined and calcined ZSF NCs.

3.3 Microstructure analysis

3.3.1 SEM analysis of rGO. As depicted in Fig. 7, an SEM image confirms the development of a layer-like structure in graphene oxide (GO). The small-sized sheets are clearly visible in the image with irregular surface morphology. Though the sample is not in the form of continuous sheets, the micro-size can be very clearly seen. The uneven distribution of GO sheets may be the cause of the surface roughness seen along the voids

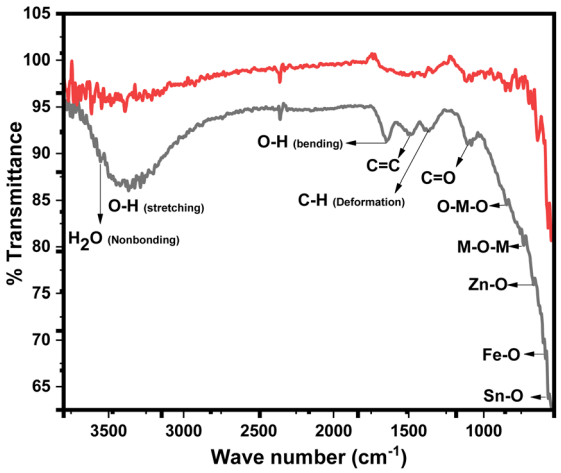

Fig. 6 FTIR spectra of uncalcined and calcined rGO-ZSF NCs.

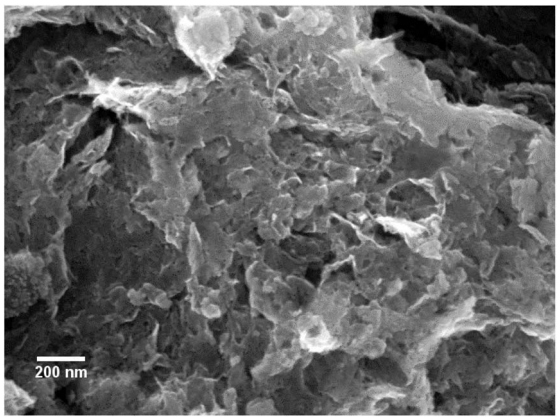

Fig. 7 An SEM image of rGO.

in the image. No sharp edges from sheets were detected in the SEM image.

3.3.2 SEM analysis of ZSF NCs. Low- and high-magnification images, as shown in Fig. 8, were obtained for the synthesized tri-metallic oxide nanocomposite comprising iron oxide, tin oxide and zinc oxide. The low-magnification image shows areas like shining stars, where many of the particles are very bright whereas many others are dull. All these bright and dull particles have formed an irregular network where the particles are irregularly distributed. To further investigate the sample morphology and other structural features, the sample was analyzed at higher magnification, which presents a close view of the particles. It is seen in the high-resolution SEM image that modest agglomeration exists in the sample, where the small particles get together to form larger aggregates with no clear boundaries. However, these larger aggregates also have a wide size range with diverse morphological shapes with clear boundaries, depending upon the number of small particles present in the larger aggregates and their arrangement. On the surface of these aggregates, a few individual particles are also present with different sizes and shapes. The cavities present in the sample because of improper particle configurations are clearer now. SEM image analysis indicates that the aggregate size ranges from 6.31 to 44.29 nm, with a mean size of 16.02 nm.

3.3.3 SEM analysis of rGO-ZSF NCs. A microstructural study of the rGO-ZSF nanocomposite was carried out using SEM, and the obtained results are depicted in Fig. 9, where separate blocks/larger cloudy aggregates are present, which are basically the graphene oxide structure with the embedded tri-metallic oxide nanocomposite. Besides some spotted particles, a few elongated particles are also seen implanted in the graphene oxide. These cloudy structures with varied sizes and shapes are randomly distributed in the studied sample, leading

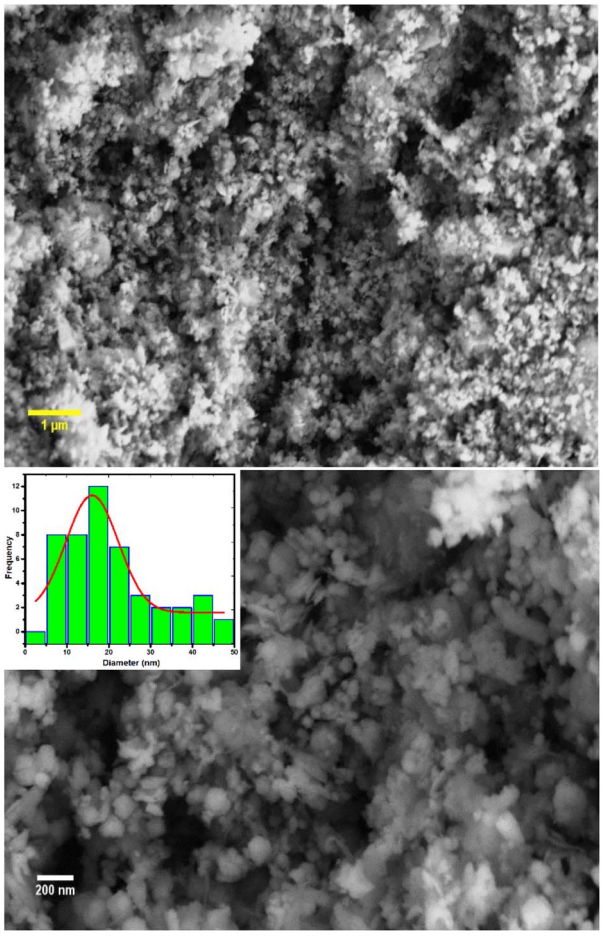

Fig. 8 Low- and high-magnification images of the ZSF nanocomposite.

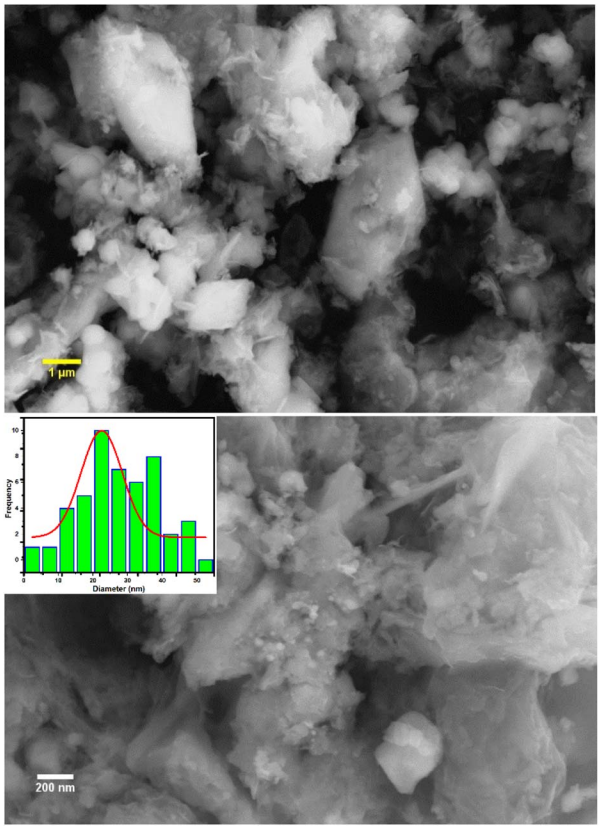

Fig. 9 Low- and high-magnification images of the rGO-ZSF nanocomposite.

to the formation of cavities. To get more information about the sample structure, the sample was also analyzed at higher resolution, which clearly shows that the solid particles are embedded in the graphene oxide matrix, where the particles are far apart from each other, suggesting that the agglomerated particles seen in Fig. 9 get separated from each other due to the stirring of the sample for a long time during synthesis. The shapes and sizes of the particles are distinct, and they are irregularly dispersed in the GO matrix. The solid particles look like stars hidden in a cloud, where some are very bright and others are dull. The dispersed particles range from 4.29 nm to 49.89 nm, with an average size of 22.5 nm.

3.4 Antibacterial activity

The antibacterial activities of calcined and uncalcined ZSF and rGO-ZSF were observed using the agar well diffusion technique against Gram-positive (*S. aureus*) and Gram-negative (*E. coli*) bacteria. The evaluation of antibacterial activity was conducted using uncalcined and calcined rGO-ZSF and ZSF nanocomposites at varying concentrations of 10, 20, 30, 40, 50, and 60 μg mL^{-1}. The ZOIs measured in mm around each well against both bacterial strains are illustrated in Fig. 10, and collected data is compiled in Table 1. The antibacterial activity enhanced upon increasing the concentration, which might be due to large amounts of sample in aqueous solution leading to more reactive species, such as metal cations and radicals, being produced by the metal oxide nanocomposites. The reactive species interact with the bacterial surface and a vital bacterial enzyme containing thiol groups, disturbing activities essential for survival and ultimately causing cell death.[35]

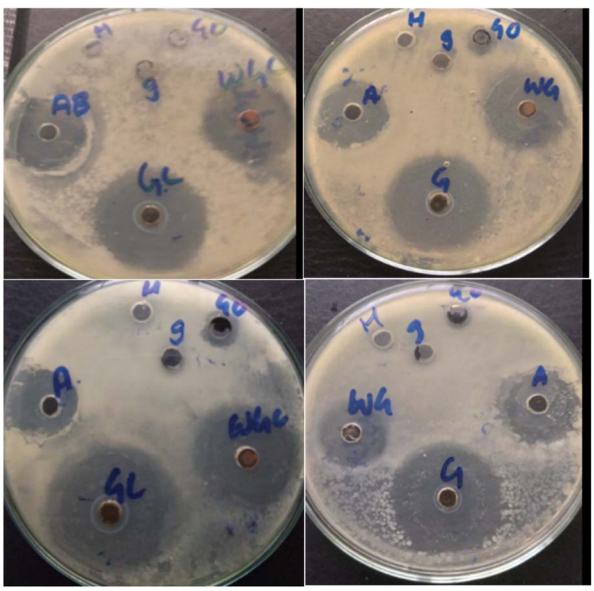

Fig. 10 Photographs of the antibacterial activities of the synthesized compounds against *S. aureus* and *E. coli*. GO = graphene oxide; A = antibiotic; g = graphite H = water; G = rGO-ZSF nanocomposite; WG = ZSF nanocomposite; GC = calcined rGO-ZSF nanocomposite; WGC = calcined ZSF NCs.

Table 1 The antimicrobial properties of uncalcined and calcined rGO-ZSF and ZSF NCs

	Inhibitory zone in millimeters (mm)	
Sample	*E. coli*	*S. aureus*
GO	7	6
Antibiotic	21	20
rGO-ZSF	31	29
rGO-ZSF (calcined)	29	27
ZSF	24	23
ZSF (calcined)	23	22

The GO-ZSF nanocomposites showed higher antibacterial activity than ZSF nanocomposites against both bacterial strains. In rGO-ZSF nanocomposites, graphene acts as a substrate and showed more antibacterial activity compared to metal oxide nanocomposites without graphene.[36] Graphene sheet edges penetrate bacterial cells upon direct contact, causing pore formation and the subsequent leakage of cytoplasmic content, which inhibits bacterial growth. Additionally, bacteria can be ensnared within the graphene sheets, leading to their inactivation.[37]

Compared to calcined rGO-ZSF and ZSF nanocomposites, the uncalcined samples are more active towards both bacterial strains, caused by the diminutive scale and greater exterior surface of the uncalcined samples, resulting in robust interactions with the bacterial cell surface. Bacterial cell viability decreased as a result, and maximal inhibition zones were detected. The particle size increased after calcination, leading to a decline in the surface-to-volume ratio. Consequently, the number of binding sites on the samples shrank, resulting in decreased interactions between the nanocomposites and bacterial surface, and minimal inhibition zones were detected.[38]

By comparing the activities of rGO-ZSF and ZSF nanocomposites against GNB and GPB, the results revealed that larger inhibition zones appeared against GNB; this may be because the chemical makeup of the bacterial cell walls differs. GPB have a thick coating of peptidoglycan in their cell walls that inhibits nanocomposites from entering the cell. On the other hand, the GNB's outer layer is made up of a thin coating of peptidoglycan that makes it easier for samples to enter the cell wall. A significant interaction between the metal cations and the negative charge of the bacterial surface may be a reason for the samples' improved anti-GNB potential. The GPB surface exhibits only partial negativity because of teichoic acid present in the cell wall, leading to poor interactions between the metal cations and bacterial surface; thus, GPB become more resistant to the examined materials.[2] Owing to the existence of lipopolysaccharides and phospholipids, the GNB surface carries a strong negative charge, providing strong binding sites for metal cations, and thus the penetrating agent encounters less resistance.[39]

Gram-positive bacteria have a thick peptidoglycan layer, while Gram-negative bacteria feature a complex outer membrane rich in lipopolysaccharides, which often acts as a permeability barrier and confers higher intrinsic resistance

against antimicrobial agents. In recent studies on MO NCs, this structural distinction is critical for evaluating the mechanism of action, as nanoparticles must overcome different structural defenses to exert their antibacterial effect, often through a combination of cell wall disruption and internal component damage.[40,41] The slowly released positively charged metal cations from the nanocomposite are electrostatically attracted to the negatively charged bacterial cell walls. Upon contact, the small size and sharp edges of the NPs can cause physical damage to the cell membrane, leading to a loss of structural integrity, the deactivation of cellular enzymes and further disruption of critical physiological functions.[42] This effect is potent against both Gram-positive and Gram-negative bacteria, though the specific interaction varies with the complexity of the cell wall structures. The combination of physical membrane disruption and ion release synergistically causes irreversible damage, resulting in the effective bacterial cell death observed.

3.5 Comparative analysis

To compare the antibacterial activity results of the current study with the reported literature against *E. coli* and *S. aureus*, the data is summarized in Table 2, showing inhibition zones of 31 mm and 29 mm, respectively, for rGO-ZSF, highlighting superior performance. The FRGO-Ag/AgO/Ag_2O and ZnO:Cu:GO composites show moderate activity (15–16 mm), while rGO-ZSF produces zones nearly twice as large. The activity of rGO-ZSF was found to be higher than those of MO and GO-integrated MO, even surpassing the performance of some silver-based GO nanocomposites. The high performance of rGO-ZSF is attributed to the synergistic combination of reduced graphene oxide (rGO) with the ZSF components, which possibly enhances the interaction with the bacterial surface and cell membrane disruption.

3.6 Antioxidant activity

Free radicals denature target molecules by stealing electrons from other molecules in order to become stable. The antioxidant potential at different concentrations of uncalcined and calcined GO, ZSF and rGO-ZSF was assessed using DPPH and ABTS free radical scavenging assays, and the data obtained is shown in Table 3 and 4. The sample absorbance was found to decline as the quantity of the sample suspension increased in the reaction. Despite the sample's lower absorbance, its capacity to scavenge free radicals increased. A higher quantity of sample contributes to greater antioxidant activity by effectively counteracting more reactive oxygen species (DPPH and ABTS radical cations).[2]

In comparison to the ZSF nanocomposite, the rGO-ZSF nanocomposite demonstrated higher antioxidant activity. This might be described in terms of radicals forming adducts on sp^2-hybridized carbon sites, causing spin to become delocalized across the conjugated graphene backbone, which then triggers radical annihilation by electron transfer and hydrogen donation from functional groups. The interactions between metal

Table 3 % RSA and IC_{50} values of uncalcined and calcined rGO-ZSF and ZSF nanocomposites from the DPPH radical scavenging assay

Sample	Concentration (mg mL^{-1})	% RSA	IC_{50}
GO	0.005	88.91	21.55
	0.010	94.16	
	0.015	96.69	
	0.020	98.25	
rGO-ZSF (uncalcined)	0.005	77.04	36.92
	0.010	85.60	
	0.015	89.88	
	0.020	94.16	
ZSF (uncalcined)	0.005	56.03	42.65
	0.010	61.28	
	0.015	68.09	
	0.020	75.87	
rGO-ZSF (calcined)	0.005	58.36	43.56
	0.010	62.64	
	0.015	72.17	
	0.020	80.73	
ZSF (calcined)	0.005	50.19	46.76
	0.010	74.51	
	0.015	83.46	
	0.020	90.66	
Ascorbic acid	0.005	68.87	25.25
	0.010	71.01	
	0.015	73.73	
	0.020	76.84	

Table 2 A comparison of the antibacterial activities of MOs and GO-integrated MOs reported in the literature with the current study

Sample	Bacterial species	Dose	Inhibition zone (mm)	Reference
CuO-NPs	*E. coli*	30 μg mL^{-1}	23	42
	S. aureus		25	
rGO-ZnO	*E. coli*	560 μg mL^{-1}	41	43
	S. aureus	22 μg mL^{-1}	20	
FRGO-Ag/AgO/Ag_2O	*E. coli*	50 μg mL^{-1}	16	44
	S. aureus		15	
GO-AgNPs	*E. coli*	3.125 g mL^{-1}	2.5	45
	S. aureus		2.5	
ZnO:Cu:GO	*E. coli*	—	16	46
	S. aureus		16	
rGO-ZSF	*E. coli*	60 mg^{-1} 3 mL^{-1}	31	Current study
	S. aureus		29	

Table 4 Percentage radical scavenging activity and IC_{50} values of uncalcined and calcined ZSF and rGO-ZSF nanocomposites from the ABTS radical scavenging assay

Sample	Concentration (mg mL^{-1})	% RSA	IC_{50}
GO	0.005	83.92	27.51
	0.010	88.59	
	0.015	92.10	
	0.020	94.73	
rGO-ZSF (uncalcined)	0.005	51.46	46.92
	0.010	77.19	
	0.015	90.35	
	0.020	93.86	
ZSF (uncalcined)	0.005	33.91	47.37
	0.010	56.14	
	0.015	72.80	
	0.020	81.87	
rGO-ZSF (calcined)	0.005	28.65	48.94
	0.010	39.76	
	0.015	61.11	
	0.020	67.83	
ZSF (calcined)	0.005	26.90	49.97
	0.010	41.23	
	0.015	64.91	
	0.020	76.60	
Ascorbic acid	0.005	42.39	43.75
	0.010	50.87	
	0.015	55.55	
	0.020	60.82	

components and graphene oxide, leading to the formation of more reactive oxygen species, is another factor for the increased antioxidant activity of graphene-based tri-metallic nanocomposites[21] These entities have the ability to transfer hydrogen atoms and electrons, causing them to react with free radicals and stabilize them.[47]

The antioxidant potential was assessed using DPPH and ABTS free radicals. For both uncalcined and calcined samples, the percentage of free radical neutralization enhanced with increasing sample amount, as illustrated in Tables 2 and 3. The uncalcined samples had a higher proportion of scavenging activity than calcined ones. The quantity of a sample needed to scavenge 50% of the radicals is known as the IC_{50} value of that sample. In comparison to the calcined samples, uncalcined samples have lower IC_{50} values, suggesting that the uncalcined samples are more active. The uncalcined samples had stronger antioxidant activity toward both ABTS and DPPH free radicals. This is due to the fact that when the temperature rises, the particle size increases and the surface area gets decreased; thus, a smaller number of free radicals can be adsorbed on the sample surface. Similarly, the number of particles in solution decreases as the particle size increases, thus providing fewer active sites to stabilize free radicals.[2,38]

4 Conclusions

The method used for the formation of GO is very simple, however it requires intense care because of its exothermic nature. The synthesis of the rGO-ZSF and ZSF nanocomposites was carried out, and they were calcined at 450 °C and analyzed *via* various approaches. The synthesis was successfully validated through XRD and FT-IR analyses. XRD results demonstrated a notable improvement in the physiochemical properties following calcination. Surface morphology analysis indicated the formation of larger aggregates with diverse sizes and shapes. Additionally, SEM analysis confirmed the embedding of metal oxides within the graphene matrix. The agglomeration initially observed in the SEM images of pure ZSF nanocomposites disappeared, likely due to the prolonged stirring of the tri-metallic oxide-graphene oxide composite, which aided in breaking down larger aggregates into individual particles. The biological efficacy of the synthesized GO, rGO-ZSF and ZSF nanocomposites and their calcined versions was assessed against *E. coli* and *S. aureus*, as well as toward ABTS and DPPH free radicals, using standard protocols. The results indicated that biological activity increased at higher sample concentrations, implying that a greater amount of sample enhances effectiveness. Among the tested materials, rGO-ZSF and its calcined counterpart exhibited the highest antibacterial activity, outperforming ZSF and its calcined form. The nanocomposites demonstrated stronger activity against *E. coli* compared to *S. aureus*. Conversely, in antioxidant assays targeting ABTS and DPPH free radicals, GO exhibited superior activity compared to the RGO-ZSF and ZSF nanocomposites and their calcined derivatives. These synthesized nanocomposites hold promise for future applications in environmental pollution remediation and catalytic processes.

Author contributions

Misbah Ashravi – formal analysis and writing – original draft; Sirajul Haq, Shafia Shujaat and Jamoliddin Razzokov – supervision, project administration, conceptualization, methodology and project administration; Maria Rashid and Ifza Ahmad – visualization and writing – original draft; Abdurahman Hajinur Hirad – software, validation and funding acquisition; Abdus Samad – data curation and writing – review & editing.

Conflicts of interest

There are no conflicts to declare associated with this study.

Data availability

The data supporting the findings of this study, including XRD patterns, W–H plots, FTIR spectra, SEM micrographs, and bioactivity measurements (antibacterial, DPPH, and ABTS assays), are available in the article and its supplementary information (SI). Supplementary information is available. See DOI: https://doi.org/10.1039/d5ra06581j.

Acknowledgements

The authors extend their appreciation to the Ongoing Research Funding Program (ORF-2025-677), King Saud University, Riyadh, Saudi Arabia.

Notes and references

1 R. Pachaiappan, S. Rajendran, P. L. Show, K. Manavalan and M. Naushad, *Chemosphere*, 2021, **272**, 128607.
2 S. Haq, P. Ahmad, M. U. Khandaker, M. R. I. Faruque, W. Rehman, M. Waseem and S. U. Din, *Mater. Res. Express*, 2021, **8**(3), 035013.
3 M. Zare, K. Namratha, K. Byrappa, D. M. Surendra, S. Yallappa and B. Hungund, *J. Mater. Sci. Technol.*, 2018, **34**, 1035–1043.
4 D. Rehana, D. Mahendiran, R. S. Kumar and A. K. Rahiman, *Biomed. Pharmacother.*, 2017, **89**, 1067–1077.
5 W. P. Xu, L. C. Zhang, J. P. Li, Y. Lu, H. H. Li, Y. N. Ma, W. Di Wang and S. H. Yu, *J. Mater. Chem.*, 2011, **21**, 4593–4597.
6 J. Ahmad and K. Majid, *Polym. Bull.*, 2021, **78**, 3889–3911.
7 E. Alsharaeh, S. Alazzam, F. Ahmed, N. Arshi, M. Al-Hindawi and G. K. Sing, *Acta Metall. Sin.*, 2017, **30**, 45–52.
8 S. Shoukat, W. Rehman, S. Haq, M. Waseem and A. Shah, *Mater. Res. Express*, 2019, **6**, 115052.
9 S. Haq, W. Rehman and M. Waseem, *J. Inorg. Organomet. Polym. Mater.*, 2018, **29**, 651–658.
10 S. Soren, S. Kumar, S. Mishra, P. K. Jena, S. K. Verma and P. Parhi, *Microb. Pathog.*, 2018, **119**, 145–151.
11 N. Bibi, S. Haq, W. Rehman, M. Waseem, M. U. Rehman, A. Shah, B. Khan and P. Rasheed, *Biointerface Res. Appl. Chem.*, 2020, **10**, 5895–5900.
12 N. Basavegowda, J. K. Patra and K. H. Baek, *Molecules*, 2020, **25**(5), 1058.
13 R. Rajeswari and H. G. Prabu, *J. Inorg. Organomet. Polym. Mater.*, 2018, **28**, 679–693.
14 A. T. Smith, A. M. LaChance, S. Zeng, B. Liu and L. Sun, *Nano Mater. Sci.*, 2019, **1**, 31–47.
15 X. Huang, X. Qi, F. Boey and H. Zhang, *Chem. Soc. Rev.*, 2012, **41**, 666–686.
16 S. Thangabalu, M. A. Sayed and M. Shkir, *Ceram. Int.*, 2025, **51**, 45555–45569.
17 V. Manikandan, G. Ayyannan, A. Kadian, K. Dev, R. S. Mane, S. Sub, M. Shkir, A. Mossad and T. Subramani, *Mater. Chem. Phys.*, 2025, **339**, 130791.
18 D. M. V Devabharathi, S. Muthusamy and T. Subramani, *Ionics*, 2025, **31**, 7177–7190.
19 P. Parthipan, M. A. Al-Dosary, A. A. Al-Ghamdi and A. Subramania, *J. King Saud Univ., Sci.*, 2021, **33**, 101438.
20 S. N. Alam, N. Sharma and L. Kumar, *Graphene*, 2017, **06**, 1–18.
21 N. Baali, A. Khecha, A. Bensouici, G. Speranza and N. Hamdouni, *C-J Carbon Res.*, 2019, **5**, 75.
22 M. J. Yoo and H. B. Park, *Carbon N. Y.*, 2019, **141**, 515–522.
23 T. Kamakshi, G. S. Sundari, H. Erothu and T. P. Rao, *Rasayan J. Chem.*, 2018, **11**, 1113–1119.
24 S. Haq, A. W. Raja, S. U. Rehman, A. Mezni, M. Ben Ali, A. Hedfi, M. I. Shahzad, W. Rehman, N. Shahzad, M. Waseem and P. Ahmad, *J. Chem.*, 2021, **1**, 3475036.
25 M. Sorbiun, E. Shayegan and M. Ali, *Int. J. Environ. Res.*, 2018, **12**, 29–37.
26 S. W. Hwang, A. Umar, G. N. Dar, S. H. Kim and R. I. Badran, *Sens. Lett.*, 2014, **12**, 97–101.
27 M. Aziz, S. S. Abbas, W. R. W. Baharom and W. Z. W. Mahmud, *Mater. Lett.*, 2012, **74**, 62–64.
28 N. C. Horti, M. D. Kamatagi, S. K. Nataraj, M. N. Wari and S. R. Inamdar, *Nano Express*, 2020, **1**, 010022.
29 Y. Wang, L. Cai, Y. Li, Y. Tang and C. Xie, *Phys. E Low-dimens. Syst. Nanostruct.*, 2010, **43**, 503–509.
30 S. Haq, S. Shoukat, W. Rehman, M. Waseem and A. Shah, *J. Mol. Liq.*, 2020, **318**, 114260.
31 F. Paquin, J. Rivnay, A. Salleo, N. Stingelin and C. Silva, *J. Mater. Chem. C*, 2015, **3**, 10715–10722.
32 S. Sultana, S. Bordoloi, S. Konwer, G. Borah and P. K. Gogoi, *Appl. Organomet. Chem.*, 2020, **34**, 1–12.
33 M. Mataji, M. Ghorbani and M. P. Gatabi, *J. Alloys Compd.*, 2018, **757**, 298–309.
34 Z. N. Kayani, F. Saleemi and I. Batool, *Appl. Phys. A:Mater. Sci. Process.*, 2015, **119**, 713–720.
35 S. Haq, H. Afsar, M. Ben Ali, M. Almalki, B. Albogami and A. Hedfi, *Crystals*, 2021, **11**, 1–12.
36 A. Ahmad, A. S. qureshi, L. Li, J. Bao, X. Jia, Y. Xu and X. Guo, *Colloids Surf., B*, 2016, **143**, 490–498.
37 H. Ji, H. Sun and X. Qu, *Adv. Drug Deliv. Rev.*, 2016, **105**, 176–189.
38 A. Hamid, S. Haq, S. Ur Rehman, K. Akhter, W. Rehman, M. Waseem, S. Ud Din, Z. ul-Abdin, M. Hafeez, A. Khan and A. Shah, *Chem. Pap.*, 2021, **75**, 4189–4198.
39 A. Shah, S. Haq, W. Rehman, W. Muhammad, S. Shoukat and M. ur Rehman, *Mater. Res. Express*, 2019, **6**, 045045.
40 T. Subramani, G. Thimmarayan, B. Balraj and N. Chandrasekar, *Inorg. Chem. Commun.*, 2022, **142**, 109709.
41 M. Mahfooz-Ur-Rehman, W. Rehman, M. Waseem, B. A. Shah, M. Shakeel, S. Haq, U. Zaman, I. Bibi and H. D. Khan, *J. Chem. Eng. Data*, 2019, **64**, 2436–2444.
42 A. Nagaveni, M. Anusuya, D. Santhanaraj, S. G. Gunasekaran, J. Gitanjali, S. Thangabalu, K. Krishnaveni and E. Jayanthi, *Inorg. Chem. Commun.*, 2024, **170**, 113503.
43 T. Naseem, A. Muhammad, W. Muhammad, H. Salah, U. Din and S. Haq, *J. Inorg. Organomet. Polym. Mater.*, 2020, **30**, 3907–3919.
44 G. S. Lekshmi, R. Tamilselvi, R. Geethalakshmi, S. D. Kirupha, O. Bazaka, I. Levchenko, K. Bazaka and M. Mandhakini, *J. Colloid Interface Sci.*, 2022, **608**, 294–305.
45 H. Kashif, M. N. Ahmed, M. Altaf, I. ul Haq, A. Iqbal and S. Haq, *Microsc. Res. Tech.*, 2024, 1–15.
46 K. Ravichandran, N. Chidhambaram and S. Gobalakrishnan, *J. Phys. Chem. Solids*, 2016, **93**, 82–90.
47 A. A. Shadmehri, F. Namvar, H. Miri and P. Yaghmaei, *Int. J. Nano Dimens.*, 2019, **10**, 350–358.